Palaeogeography, Palaeoclimatology, Palaeoecology 624 (2023) 111654

Contents lists available at ScienceDirect

Palaeogeography, Palaeoclimatology, Palaeoecology

journal homepage: www.elsevier.com/locate/palaeo

Paleoclimatic and anthropogenic impacts on the environment of Southwest China since 33 ka based on multiproxy analysis of karst depression deposits

Xing Tian [a], Xiaoyong Long [a], Shu'e Luo [a], Min Cao [b], Ji Li [a], Yuchuan Sun [a], Sibo Zeng [a], Ze Wu [a], Chuan Liu [a], Lidan Lei [a], Thomas J. Algeo [c,d,e], Yongjun Jiang [a,*]

[a] Chongqing Key Laboratory of Karst Environment & School of Geographical Sciences, Southwest University, Chongqing 400715, China
[b] School of Earth Sciences, Yunnan University, Yunnan 650500, China
[c] State Key Laboratory of Geological Processes and Mineral Resources, China University of Geosciences-Wuhan, Wuhan, China
[d] State Key Laboratory of Biogeology and Environmental Geology, China University of Geosciences- Wuhan, Wuhan, China
[e] Department of Geosciences, University of Cincinnati, Cincinnati, OH, USA

ARTICLE INFO

Editor: S Shen

Keywords:
Pleistocene
Holocene
Chemical index of alteration
Radiocarbon dating
Grain size
Guangxi

ABSTRACT

Paleoclimate change and anthropogenic activities have fundamentally modified the Earth's environmental system since the late Quaternary. Southwest China has one of the largest continuous karst areas in the world, yielding geological records from karst depressions that can improve our understanding of changes in the dominant control on regional environmental conditions. In this study, we investigated a sediment sequence formed over 33,000 years in a typical karst catchment by using combined geophysical, geochemical and biological properties of the depression deposits. The results suggest that paleoclimate change was the main modulator of environmental changes prior to the Late Holocene, and that significant vegetation change related to paleotemperature influences played an important role during the Early (ca. 12–8 ka) and Middle (ca. 8–4 ka) Holocene. During the Late Holocene (ca. 4–0 ka), the impact of anthropogenic activities has overwhelmed paleoclimatic influences on the environment. This study demonstrates the utility of dated karst depression deposits for reconstructing Holocene climate change and the timing of anthropogenic impacts on the landscape.

1. Introduction

The influence of anthropogenic activities on Earth systems has increased gradually through time (Wan et al., 2015). Although the start of the Anthropocene has been set at 1950 CE by the Anthropocene Working Group (AWG) (Syvitski et al., 2020; Waters and Turner, 2022), various studies have demonstrated that anthropogenic influences on the landscape, which were related to population migration, agriculture and deforestation, have been pronounced since the Late Neolithic (ca. 4–5 ka; note: ka = kyr BP) (Jenny et al., 2019; Mottl et al., 2021; Ruddiman et al., 2020; Zhang et al., 2022). The scope of anthropogenic impacts can be systematically observed and studied only for the past few centuries, hindering a precise evaluation for earlier time intervals (Jenny et al., 2019; Ruddiman et al., 2020). High-resolution geological records are therefore needed to address this issue.

Sediments from karst landscapes in Southwest China, spanning six provinces (Guangdong, Yunnan, Sichuan, Hubei, Hunan, and Guizhou), an autonomous region (Guangxi), and a city directly under the Central Government (Chongqing), are highly sensitive to anthropogenic activities and Asian Monsoon (AM) changes. High-resolution geological records in Southwest China, such as stalagmites and lake sediments, have been widely used for reconstructing paleoclimate change during the Quaternary (a key period in the birth and rapid development of mankind). For example, cave stalagmite $\delta^{18}O$ records have shown that an external driver (i.e., solar radiation) dominated AM variation on orbital timescales until the mid-Holocene (Cheng et al., 2016; Wu et al., 2020), whereas pollen records from lake sediments have shown that the climate shift in Southwest China from humid conditions in the Early and Middle Holocene to drier conditions in the Late Holocene occurred abruptly at ca. 4.5 ka, in conjunction with increasing anthropogenic influences (Ren, 2007; Zhao et al., 2009).

The history of anthropogenic influences in Southwest China has been reconstructed through archaeological studies. An archaeological meta study revealed an initial peak in the number of archaeological sites in Southern China at ca. 4–5 ka, followed by a further substantial increase after ca. 3450 yr BP (Hosner et al., 2016). Southern China has served as

* Corresponding author.
E-mail address: jiangjyj@swu.edu.cn (Y. Jiang).

https://doi.org/10.1016/j.palaeo.2023.111654
Received 21 March 2023; Received in revised form 20 April 2023; Accepted 24 May 2023
Available online 29 May 2023

an important breadbasket throughout dynastic Chinese history, and the spread of agriculture to this region can be traced back even further in time. In the middle and lower Yangtze valley, rice domestication began at 8950–7950 yr BP (Fuller et al., 2008; Zhao, 2010), >3000 years before it spread into Southwest China (Guedes et al., 2013). Despite the long history of agriculture in Southwest China, high-resolution geological records have only rarely been utilized to reconstruct the history of anthropogenic activities, largely because of uncertainty regarding human impacts on the geophysical, geochemical and biological properties of karst depression deposits when combined with natural processes.

Karst covers a cumulative area of 3.44 million km^2 in China (predominantly in Southwest China), representing about 36% of the total land area of China and 15.6% of the 22 million km^2 of karst terrain globally (Jiang et al., 2014). Karst depressions, which are some of the most common landforms in karst regions, are negative landforms that arise from the collapse of underground caves, or the dissolution of soluble lithologies, such as limestone, dolomite, and gypsum, facilitated by high temperatures and precipitation levels in tropical and subtropical climates. Karst depressions accumulate deposits that are easily affected by an assortment of climatic and human processes, and they can therefore provide substantial information about not only paleoclimate change but also the historical human role in the accumulation of these sediments. For example, previous studies have reconstructed soil loss from karst catchments in Southwest China by using dated depression deposits (Bai et al., 2010; Zhang et al., 2020), and multiproxy studies have yielded insights into the geoarchaeological history of karst mountains in Crete (Siart et al., 2010). As such, karst depression deposits in Southwest China offer a unique opportunity for paleoclimatic and archaeological studies, making them promising geoarchives, particularly in regions without any lacustrine and stalagmite records. However, previous studies of depression deposits have not taken into account long-term (>10 kyr) anthropogenic and paleoclimatic impacts on karst environments.

In this study, two typical karst depressions in Southwest China were selected for generation of a multiproxy dataset to investigate the anthropogenic and paleoclimatic impacts on environmental changes in karst systems. The objectives of the present study are: (1) to test the reliability of the AMS ^{14}C dating method for karst depression deposits; (2) to reconstruct the long-term history of paleoclimate change and anthropogenic activities in the study region, and (3) to delimit the timing of anthropogenic impacts on the landscape. This work has the potential to make significant advances in our understanding of long-term climate-human-environment interactions in karst regions, representing one of the first attempts to use karst depression deposits for this purpose.

2. Regional setting

The study area is located in Daliang Town, Rong'an County, Liuzhou City, Guangxi Autonomous Region, Southwest China. The area is a peak-cluster depression landscape with strong karst features known as the Guancun Depressional Complex (Fig. 1A-B). It has a moist subtropical monsoonal climate with a high mean annual rainfall (1750 mm) and

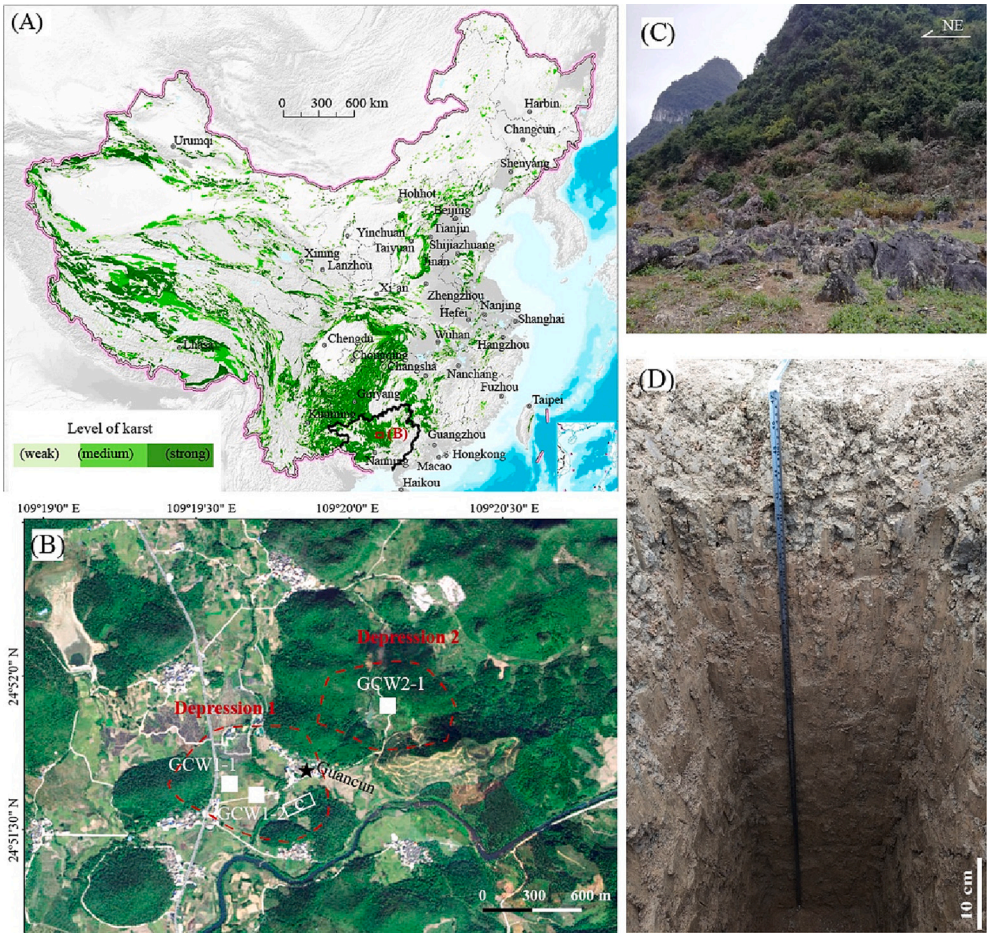

Fig. 1. Background of the study area. (A) Map of carbonate rock distribution with level of karst development in China, modified from Sun et al. (2020), showing location of the study area (black outline of Guangxi Autonomous Region); (B) study sites in the Depression 1 and 2, which are two representative depressions in the Guancun Depressional Complex; (C) representative landscape of the study area; and (D) representative sediment pit near the GCW1–2 drillcore.

temperature (20 °C). Precipitation is the main source of water in this area, and runoff is the major vector of sediment transport. Almost 60% of rainfall occurs in summer. Elevations of this region range from 160 to 420 m above mean sea level. The Quaternary sediments and soils are underlain by Permian and Carboniferous limestones that are well exposed, with some hillslopes showing severe soil erosion or karst rocky desertification (KRD) (Fig. 1C).

According to the historical records of Rong'an County (Chen, 1996), the study area has a long history of human occupation, agriculture and mining. Population numbers increased exponentially after the Tang dynasty (1332–1043 yr BP). Due to the poor drainage capacity of the underground fissures and caverns in the study area, sediments transported by runoff from the surrounding mountains and hills to the depressions accumulated with few losses. The hillslope vegetation is primarily composed of low forests and shrubs, exhibiting features of reduced vegetation cover, significant soil erosion, and ecosystem fragility (Fig. 1C). Conventional tillage practices in Rong'an County have remained unchanged over time, relying heavily on manual labor (Chen, 1996). The agricultural activities involve using a mini-type mold-board plough to cultivate fields to a depth of approximately 15 cm, followed by crop sowing, harrowing, and rolling. The fields are inundated in April, fertilized and planted with rice in May, and after the rice harvest in August, most of the fields are replanted with vegetables or cereal grains until March of the following year.

For this study, a number of pits were dug and drillcores taken to examine the sediment fill of depressions across the Guancun Depressional Complex. In this report, we will focus on the results of the three longest drillcores, which were recovered from two karst depressions: Depression 1, which has depression and catchment areas of ~16 ha and ~ 32 ha, and Depression 2, with corresponding values of ~5 ha and ~ 20 ha, respectively (Fig. 1C). Cores GCW1–1 (24°51′26.05″N, 109°19′52.30″E) and GCW1–2 (24°51′26.12″N, 109°19′59.18″E) were taken from the margin and center of Depression 1, respectively, and core GCW2–1 (24°51′41.82″N, 109°20′22.43″E) was taken from the center of Depression 2. The three cores were sampled at 2 cm intervals through the uppermost 60 cm, and then at 5 cm intervals below that level. The total thicknesses of sections GCW1–1, GCW1–2 and GCW2–1 are 220, 505, and 500 cm, respectively, in each case reaching the bedrock at the base of the karst depression.

Despite differences in size, Depressions 1 and 2 have similar sediment fill patterns. In each depression, the thickness of the sediment fill increases gradually from its periphery to a maximum of ~6 m in its center. This suggests that sedimentation within the depressions was influenced by the same factors, i.e., topography and hydrology. Although the traditional depth of tillage is ~15 cm, modern human agricultural practices have disturbed the upper layer of sediment in the depressions up to ~30 cm below the ground surface. Below this depth, there are generally few human artifacts or evidence of tillage (Fig. 1D).

3. Materials and methods

A total of 124 samples (3 from GCW1–1, 118 from GCW1–2, and 3 from GCW2–1) were collected for this study. Each sample was initially air-dried and roughly crushed by hand to remove roots and other debris, before being hand-sieved through a 2-mm sieve. Afterwards, the samples were further crushed using an agate mortar and pestle and passed through mesh sieves of varying apertures. Samples for particle size analysis were left uncrushed, while those for dating and $\delta^{13}C_{org}$ analysis were crushed and passed through a 100 mesh (0.15 mm) sieve. Samples intended for elemental and TOC analyses were further crushed and passed through an 80 mesh (0.18 mm) sieve.

Accelerator Mass Spectrometry (AMS) ^{14}C dates were measured on bulk organic matter in the three sections because few charcoal deposits were found in the excavated sections. As GCW1–2 is located at the center of a depression and represents the deepest profile, we focused dating efforts on this profile. Before AMS ^{14}C counting, each sample was first pretreated with a total acid wash to remove carbonates, and ensure that only the carbon fraction of interest (i.e., bulk organic carbon) was analyzed. A total of 17 samples from GCW1–2, 3 samples from GCW1–1, and 3 samples from GCW2–1 were selected for AMS ^{14}C dating and $\delta^{13}C_{org}$ analysis. All of the ^{14}C dates were calibrated with the IntCal 20 calibration curve by using an R package of Clam (Blaauw, 2010; Reimer et al., 2020). The average sedimentation rates are equal to the slope of the best-fit lines through the measured ages. AMS ^{14}C dating and $\delta^{13}C$ measurements were performed by Beta Analytic Inc., USA, following their standard laboratory procedures (https://www.radiocarbon.com/beta-lab.htm).

The absolute sediment particle size and the total organic carbon (TOC) content of 118 samples of GCW1–2 were determined by using a laser particle size analyzer (Mastersizer 2000, Malvern, UK) and Multi N/C 3100 TOC/TN analyzer (Analytik Jena GmbH, Jena, Germany), respectively. Experiments were conducted at Chongqing Key Laboratory of Karst Environment, Southwest University, China. For the particle size, approximately 0.3 g of each sample was pretreated with 10 mL of 10% H_2O_2 to remove the organic matter, and 10 mL of 10% HCl to remove the carbonates. Then deionized water was added to the sample solution and held for ~24 h to rinse acidic ions. Finally, the sample residue was treated with 10 mL of 10% sodium hexametaphosphate ($(NaPO_3)_6$) on an ultrasonic vibrator for 10 min to facilitate dispersion of aggregates before grain-size analysis.

The Mastersizer 2000 yields the percentages of particle size fractions and median particle sizes of the sample with a relative error of <1%. Each sample was tested three times with a measurement range of 0.01–10,000 μm, followed by calculation of the mean particle content and mean grain size. For TOC analysis, approximately 50 mg of the pulverized sample (pre-treated with hydrochloric acid to remove the inorganic carbon fraction) was placed on a ceramic boat, and then heated to a temperature of 1200 °C to determine TOC content by combustion analysis.

Major and rare earth elemental analyses were performed on 99 bulk samples at the laboratory of ALS Chemex Co Ltd. (Guangzhou, China) and Chongqing Key Laboratory of Karst Environment (Chongqing, China), respectively. Major elements were analyzed by X-ray fluorescence analysis (XRF) using fused glass disks. Loss-on-ignition (LOI) was determined by the weight difference after ignition at 1000 °C in a muffle furnace. The concentration of rare earth elements was determined using single-collector inductively coupled plasma mass spectrometry (Thermo Element XR, USA). About 50 mg of powdered samples were dissolved and sequentially digested using a standard HF-HNO_3-$HClO_4$ protocol, and the final solution was diluted with 2% nitric acid for ICP-MS analysis. The chemical index of alteration CIAm (a modified form of CIA; Nesbitt and Young, 1982), where "m" indicates minus CaO (Arnaud et al., 2012) were generated per the following equations:

$$\mathrm{CIAm} = \frac{Al_2O_3}{(Al_2O_3 + Na_2O + K_2O)} \times 100\% \quad (1)$$

4. Results

4.1. AMS ^{14}C dating

Radiocarbon (AMS ^{14}C) dating is currently the most common and precise method to date sediments as old as ca. 55 ka (Cheng et al., 2018a). The chronology in this study was supported by 23 AMS ^{14}C dates of the bulk organic fraction of samples (Fig. 2A), and all of these dates were separately calibrated with the IntCal 20 calibration curve. GCW1–1 and GCW2–1 yielded simple age progressions with depth, based on a small number of dates ($n = 3$ for both cores), that are readily modeled with linear regressions. The dates obtained from GCW1–1 and GCW2–1 exhibit increasing trends with depth (Fig. 2B-C), with dating errors ranging from 30 to 80 years (as given in Supplementary Table S1). Owing to the restricted number of dates, the uncertainties in the age

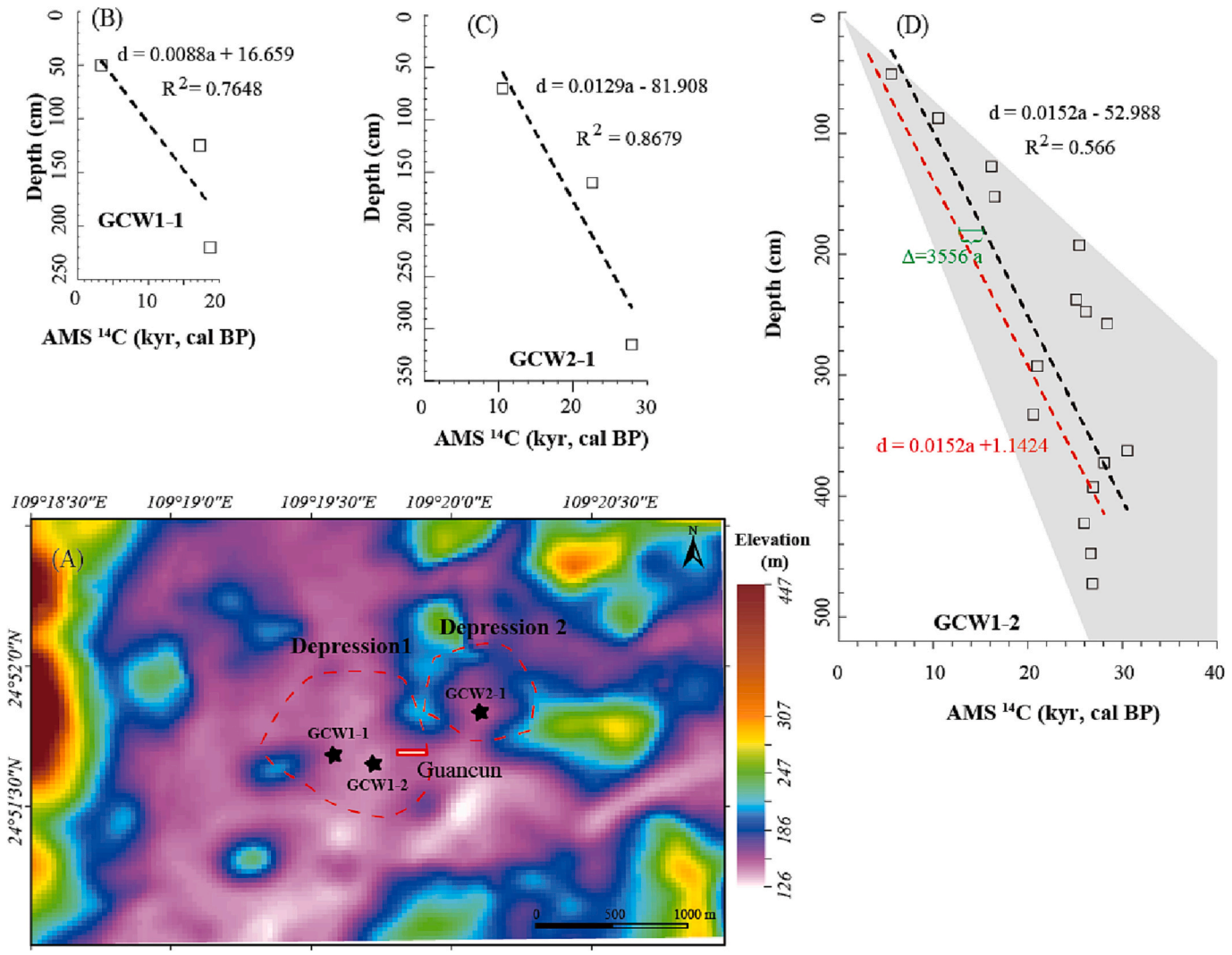

Fig. 2. Age-depth model of the profiles from Guancun Depressional Complex based on calibrated radiocarbon dates. (A) Elevation map showing the two study depressions and three sampling sites. Age-depth models for (B) GCW1–1, (C) GCW2–1, and (D) GCW1–2. BP: before present (1950 CE). In C, the shaded area represents uncertainty in age-depth relationships, which increases with depth.

models of GCW1–1 and GCW2–1 are relatively minor, which were roughly defined as the areas between the maximum and minimum slope fitting curves in this study.

The calibrated AMS ^{14}C dates for GCW1–2 (n = 17; given in Supplementary Table S1) suggest deposition of the sediments in Guancun Depressional Complex at least as far back as the Late Pleistocene. The dates obtained from GCW1–2 also exhibit an increasing trend with depth (Fig. 2D), with dating errors ranging from 30 to 110 years (refer to Supplementary Table S1 for details). Although GCW1–2 contains some age anomalies (i.e., older dates higher in the profile than younger dates), the full AMS ^{14}C dataset for this profile shows a systematic pattern of older ages with depth (Fig. 2D). The reversed ages may be caused by dating bulk organic matter instead of a specific sediment fraction (e.g., charcoal) as in more closed systems (e.g., deep lake or marine) (Heaton et al., 2021; Zhou et al., 2022).

The consistency of the sedimentation rates observed among the study sites supports the reconstructed chronologies. GCW1–1, which is located on the margin of Depression 1 (Fig. 2A), has a mean sedimentation rate of ~9 cm/kyr (Fig. 2B). In contrast, GCW2–1 and GCW1–2, which are located in the centers of their respective depressions, show higher sedimentation rates, i.e., ~13 cm/kyr (Fig. 2C) and ~ 15 cm/kyr (Fig. 2D), respectively. Moreover, the sedimentation rates of this study can be compared with the mean sediment accumulation rates (SARs) of lakes and peatlands in China (0.37–22.4 cm/kyr; Zhang et al., 2022) and with deposits from other karst depressions in Guangxi (2.6–77 cm/kyr; Wu, 2021). Using a surface age of 2020 CE as a reference, we applied a uniform offset of 3356 years (i.e., to correct for the effects of dead carbon on radiocarbon ages) to establish an appropriate age-depth model for GCW1–2. Although the sources of errors in individual dates are uncertain, the AMS ^{14}C dataset as a whole offers a robust age model for the study profiles.

4.2. Grain-size analysis

Particle size distributions (PSDs) are controlled by sediment sorting during transport, and various particle size fractions were used as hydroclimatic proxies in this study. The PSDs were generated for the depression deposits by separating them into 3 grain-size fractions: clay (< 0.002 mm), silt (0.002–0.02 mm), and sand (0.02–2 mm). For GCW1–2, the PSDs, mean and median particle sizes vary with depth (Fig. 3). Both the mean and median particle sizes show similar, strong correlations with the sand fraction (R^2 = 0.98). Silt makes up the bulk of the depression deposits, ranging from 45% to 70%, but exhibits a relatively smaller coefficient of variation than sand (CV = 0.09, Supplementary Table S2). The clay content ranges from 5% to 37%, and the sand content ranges from 4% to 59%. All PSDs are unimodal

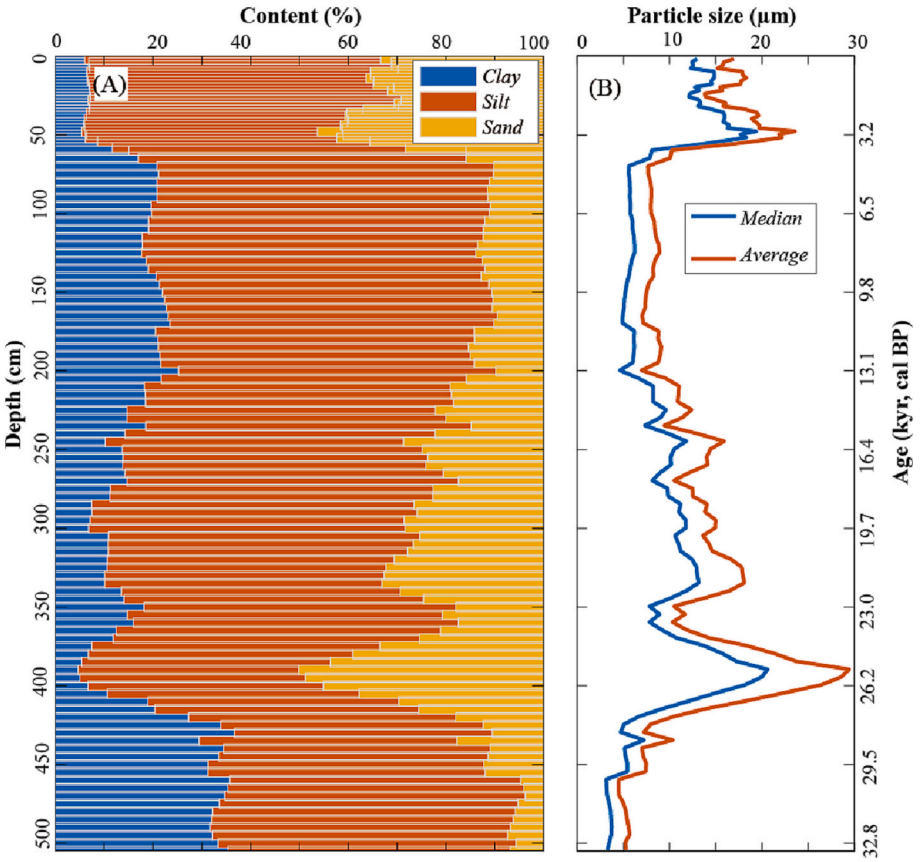

Fig. 3. Profiles for GCW1–2. (A) Stacked PSDs, and (B) variation of mean and median particle sizes. The proxies are plotted versus depth (left axis) and time (right axis).

(Supplementary Fig. S1), suggesting a single source for each size fraction. The largest particle in all samples is <800 μm, and the mean particle size of the study deposits is only 13 μm, suggesting that the majority of the sediment grains in both eolian and fluvial facies was transported as a suspended fraction (Ge et al., 2020).

4.3. Elemental proxy analysis

In this study, elemental ratios such as the CIAm, Al/K, Na/K, Al/Na, and La/Sm were used as proxies for chemical weathering intensity. The trends of all proxies for chemical weathering intensity fluctuate greatly with depth and time, being either in-phase or anti-phased with each

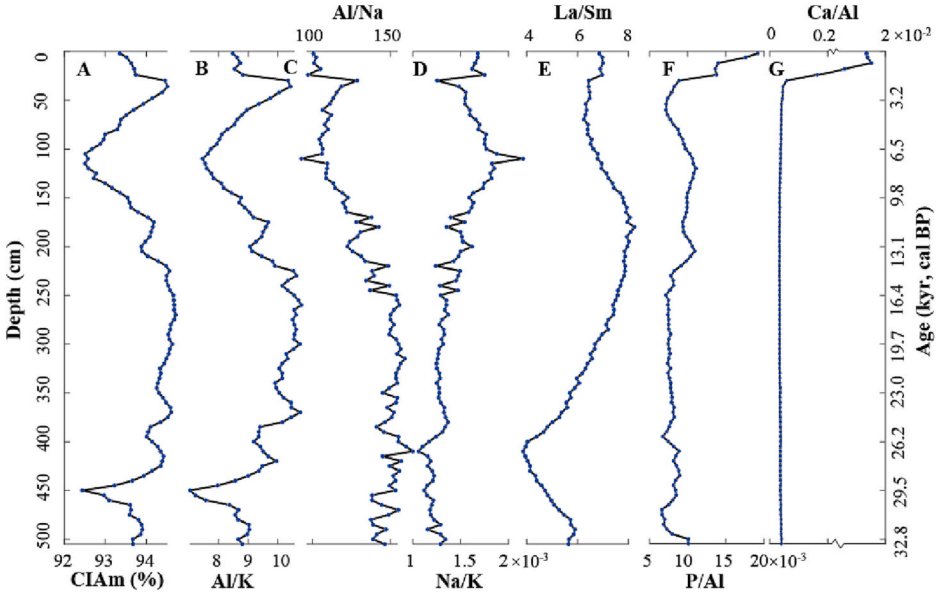

Fig. 4. Geochemical profiles for GCW1–2. (A) CIAm, (B) Al/K, (C) Al/Na, (D) Na/K, (E) La/Sm, (F) P/Al, and (G) Ca/Al. Profiles A-E are proxies for chemical weathering intensity, whereas profiles F and G are proxies for anthropogenic activities. All proxies are plotted versus depth (left axis) and time (right axis).

other (Fig. 4A-E). The abrupt increase in CaO above the depth of 60 cm may be due to carbonate nodule formation (i.e., through natural hydrological processes) and/or deep modern tillage practices (which can disturb the sediment to a depth of 30 cm, potentially mixing chips of carbonate bedrock into the soil). In order to eliminate this sudden lithology-related change, we adopted CIAm in place of CIA (Fig. 4A) as a composite proxy for chemical weathering intensity. CIAm is relatively stable, averaging 93.9 and ranging from 92.4 to 94.7.

Previous studies have demonstrated the utility of phosphorus (P) as a proxy for anthropogenic influences at archaeological sites (Monge et al., 2016; Tiessen, 1996). Higher levels of P generally indicate larger amounts of organic matter, reflecting a greater intensity of human occupation and/or activity (Marwick, 2005; Schlezinger and Howes, 2000). In the present study profiles, P content averages 886 ppm, ranging from 54 to 1350 ppm. Given the absence of measurable calcium phosphate bone remains in the profile, it is likely that P in this study site is present in the forms of adsorbed P, organically complexed P, or mineral-bound P. Therefore, the ratio of P/Al was used to reconstruct the anthropogenic activities (Fig. 4F). Calcium (Ca), which commonly co-occurs with P, is also useful as a proxy for anthropogenic influences (Oonk et al., 2009). In the study site, Ca content averages at 0.67%, ranging from 0.35% to 6.54%, which is significantly higher than the background value of Ca (0.13%) in Guangxi (China National Environment Monitoring Centre, 1990). The high content and gradual increase of Ca is likely due to the weathering of parent carbonate rocks, while the abrupt increase in Ca content in the top may be attributed to anthropogenic activities (Fig. 4G). To eliminate the dilution effects, Ca/Al was also used as a proxy similar to P/Al. The trends of these element ratios (Fig. 4F-G) are similar, with relatively stable amounts below 60 cm (i.e, prior to ca. 4 ka) followed by rapid increasing toward the top of each profile.

4.4. Total organic carbon (TOC) and $\delta^{13}C_{org}$

Sediment $\delta^{13}C_{org}$ and TOC can be used as proxies for vegetation changes and bioproductivity (Li et al., 2012). The majority of the organic matter in sediments and soils consists of humic substances, which account for 2–8% of the solid materials and are mainly derived from decaying plants and microorganism residues (Qu et al., 2022). As vegetation grows and dies, it contributes to the accumulation of organic matter in depression deposits, TOC therefore is potentially a useful proxy for changes in bioproductivity. $\delta^{13}C_{org}$ in sediments can be used as a proxy for the relative abundances of the ^{13}C-enriched (i.e., C_4 plants) and ^{13}C-depleted (i.e., C_3 plants) components of vegetation, which commonly mirrors the proportions of grasses and trees/shrubs, respectively (e.g., Liu et al., 2018). In this study, both TOC and $\delta^{13}C_{org}$ exhibit relatively simple patterns of variation with depth and time. The $\delta^{13}C_{org}$ values range from −26.2‰ to −22.7‰ (Fig. 5A), and the TOC values from 0.25 to 3.78% (Fig. 5B). $\delta^{13}C_{org}$ values remain relatively stable below a depth of 257 cm (equivalent to ca. 16.8 ka), becoming higher above this level. TOC is relatively low and uniform below a depth of 75 cm (equivalent to ca. 4.8 ka), but exhibits an exponential increase above it. These observations suggest that there have been changes in vegetation and bioproductivity in the study area during the Holocene.

5. Discussion

5.1. Vegetation changes since the Late Pleistocene

Previous studies in Southwest China have inferred a landscape vegetated by cold and dry alpine forests and grasses during the Late Pleistocene, with a decline in the areal cover of warm and moist forests during the Holocene. For example, based on a compilation of pollen data from north of the Yangtze River, Ren (2007) reconstructed changes of forest cover, finding that the vegetation cover decreased from ~95% to ~60% in the Yangtze-Huaihe area but increased from ~50% to ~85% in Northeast China during the Holocene. Based on fossil pollen records from 31 sites, Zhao et al. (2009) found that Southwest China was dominated by subtropical broadleaf evergreen and deciduous forest and tropical monsoonal rain forest during the Holocene. However, the paleoclimate in Southwest China was cool and dry during the Late Pleistocene, and the temperate deciduous broadleaf forest, pure warm-temperate evergreen forest, tropical semi-evergreen and evergreen broadleaf forests during the Holocene Epoch were restricted or absent, with vegetation in this area instead being dominated by alpine trees (e.g. *Pinus, Abies, Picea* and *Betula*) and grasses (Cheng et al., 2018b; Ni et al.,

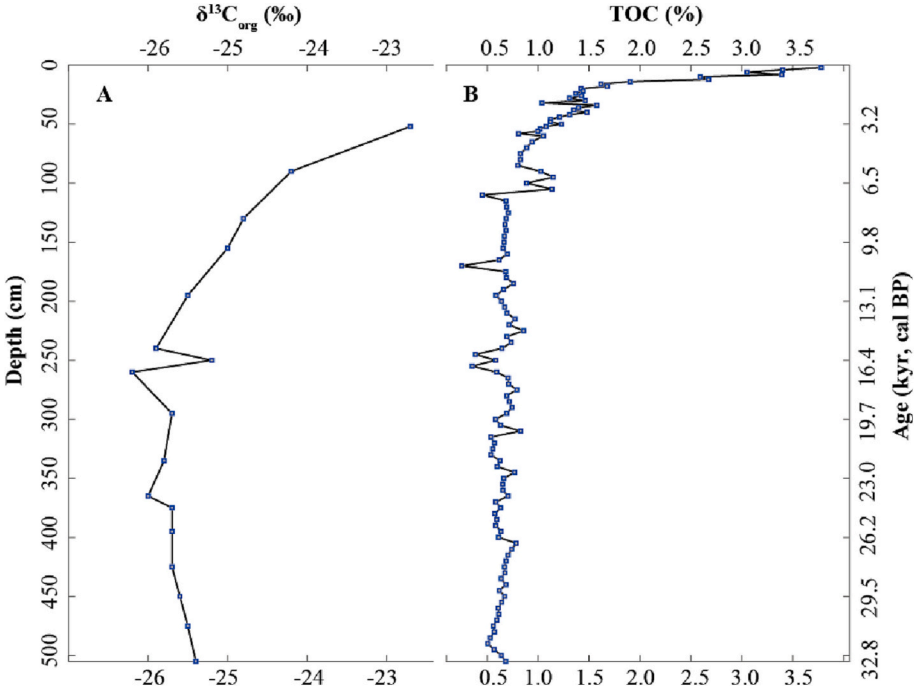

Fig. 5. Profiles for GCW1–2. (A) $\delta^{13}C_{org}$, and (B) Total organic carbon (TOC) plotted as a function of depth (left) and age (right).

2010; Sun et al., 1986).

Paleotemperature may have controlled the vegetation changes before the Late Holocene in the AM-influenced study area (Li et al., 2019). To test this hypothesis, we use mean annual air temperatures (MAAT) reconstructed from lake sediments in Yunnan Province (Zhao et al., 2021; Fig. 6A) and vegetation changes reconstructed from pollen in Guangdong Province (Wang et al., 2007; Fig. 6B) (i.e., near to the study area) to compare with the $\delta^{13}C_{org}$ (Fig. 6C) and TOC (Fig. 6D) profiles of this study. These records show a rough subdivision into cool and warm conditions based on MAAT (Fig. 6A), as well as shorter-term cool (i.e., Last Glacial Maximum (LGM), Older Dryas (OD), Younger Dryas (YD), and Heinrich stadials 1–3 (H1,H2,H3)) and warm episodes (i.e., the Bølling-Allerød interstadial (BA) and Holocene Optimum (HO)). In this study, given the limited evidence available, it is challenging to discuss these short-term paleoclimate events. Therefore, we will focus on the longer-term intervals (i.e., >1 kyr) of alternately cool and warm conditions based on the data generated herein.

Previous studies have shown that the $\delta^{13}C_{org}$ of modern deposits commonly records the isotopic composition of local vegetation (Li et al., 2012; Zhou et al., 2019), although caution must be exercised owing to considerable variation in the nature of vegetation cover in space and time. During the Holocene, increased paleotemperature and decreased vegetation cover correspond to increased $\delta^{13}C_{org}$ values, suggesting control of vegetation cover by climatic conditions, as well as a good causal relationship between the $\delta^{13}C_{org}$ and the reconstructed vegetation cover (Wang et al., 2007; Fig. 6A), with greater C_3 plant cover during cool humid intervals and greater C_4 plant cover during warm dry intervals (cf. Chen et al., 2021; Li et al., 2017).

Although few vegetation data have been reported from Southwest China for the Late Pleistocene, the relative uniformity of the temperature, $\delta^{13}C_{org}$ and TOC profiles likely implies a relatively stable vegetation cover at that time. Transitions between cool and warm climate conditions, from the onset of OD to the termination of BA, are marked by significant fluctuations in $\delta^{13}C_{org}$ and TOC content. These fluctuations indicate that the vegetation may have undergone significant changes during such transitions. To gain a more comprehensive understanding of this relationship, high-resolution records are required for further investigation. However, the overall strong correlations between variations in MAAT, vegetation cover, and the $\delta^{13}C_{org}$ and TOC proxies indicate that paleotemperature played a dominant role in controlling vegetation changes in the study area during the Late Pleistocene to Holocene.

Anthropogenic activities may also have exerted strong influence on vegetation changes during the Late Holocene (Ren, 2007). Paleotemperatures show a marked decrease at ca. 4 ka before increasing after ca. 2 ka, but the area of vegetation cover in adjacent areas and TOC values continued to rise, an observation that therefore raises a question concerning the primary driver of paleotemperature change during this

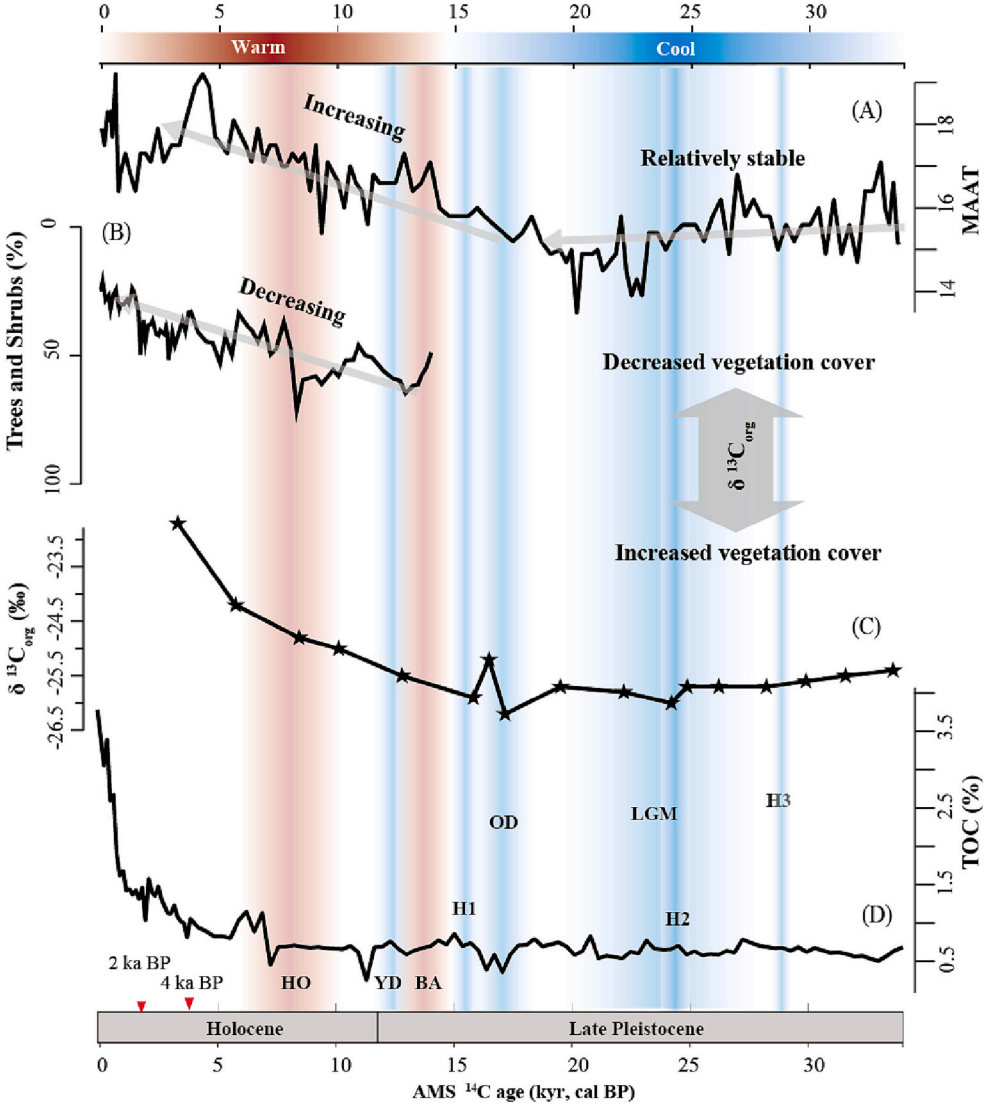

Fig. 6. (A) Mean annual air temperature (MAAT) reconstructed from maar lake sediments in Yunnan (Zhao et al., 2021); (B) Percentage of trees and shrubs, based on pollen records in Guangdong (Wang et al., 2007), note the inversed vertical axis; (C) and (D) $\delta^{13}C_{org}$ and TOC (this study). At top, the horizontal band shows intervals of generally cooler (35–15 ka) and warmer (15–0 ka) conditions, based on MAAT and paleoclimatic events. Below, the vertical blue and red bands represent short-term cool and warm episodes, respectively. (For interpretation of the references to colour in this figure legend, the reader is referred to the web version of this article.)

time interval. These results agree with inferences that declining Chinese forest cover since the Late Holocene was most probably due to anthropogenic activities (Ren, 2007), but the magnitude and precise timing of forest loss are not clear and require further investigation (Zhao et al., 2009).

5.2. Paleoclimate change before the Late Holocene

PSDs and elemental ratios are great proxies for paleoclimate change. For example, previous studies have made extensive use of PSDs in loess, paleosols, and lake sediments as proxies for the AM, yielding reconstructions of East Asian Monsoon (EAM) variability since the

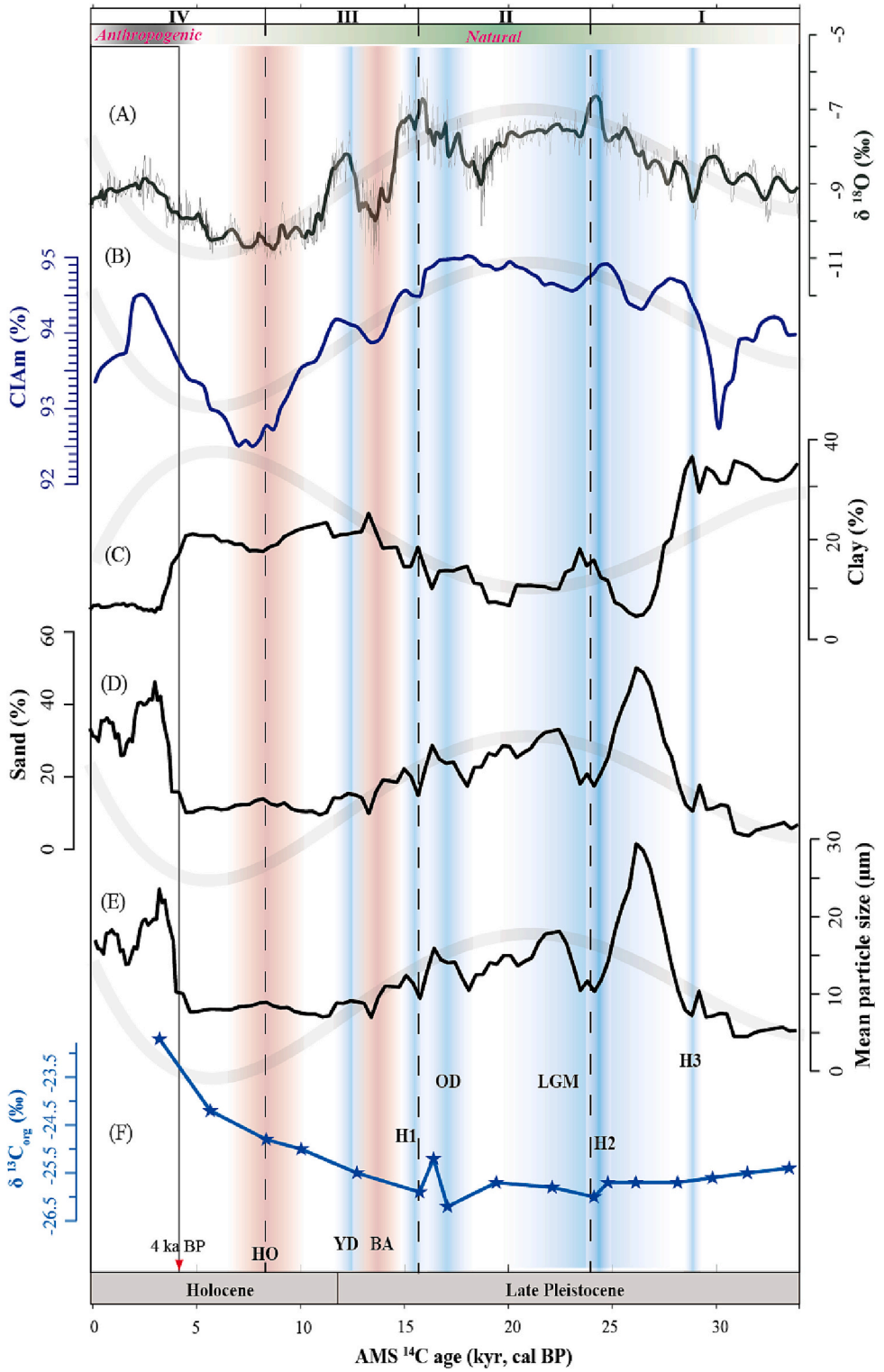

Fig. 7. Comparison of long-term multiproxies with cave $\delta^{18}O$ records over the past 33 kyr. (A) Composite stalagmite $\delta^{18}O$; (B) CIAm; (C) clay fraction; (D) sand fraction; (E) mean particle size; and (F) $\delta^{13}C_{org}$ records. All data from this study except stalagmite $\delta^{18}O$ (from Cheng et al., 2016). The thick gray lines in A-E represent the best quartic polynomial fit to stalagmite $\delta^{18}O$ (A).

Holocene (Peng et al., 2005), the Pleistocene (Lu and An, 1999) and over longer time intervals (Guo et al., 2008; Lu and Guo, 2014; Sun et al., 2010). The chemical index of alteration (CIAm) (Arnaud et al., 2012) is widely used to infer changes in regional chemical weathering intensity, which is also largely related to regional changes of AM intensity (Wei et al., 2006). Considering the monsoonal climate of the study area, we can reasonably assume that the PSDs and CIAm in the karst depressions are potential proxies for changes in AM intensity.

Primary (i.e., clay, silt, and sand) and aggregated particles commonly have different transport histories (Rienzi et al., 2013). As the cohesive force of clay minerals is strong, clay-sized particles were prone to transport as silt- or sand-sized aggregates that were mobilized primarily under strong hydrodynamic flow conditions and that experienced transport as bedload components (Schieber et al., 2007). Although some weak aggregates may have disintegrated during transport due to turbulence (Meyer et al., 1992), the degree of particle aggregation can increase with the total clay content of the original sediment or soil (Wang and Shi, 2015). In contrast, coarser size fractions (e.g., silt and sand) are generally dispersed and transported as separate particles (Wang et al., 2014). Therefore, more clay content could probably mean higher hydrodynamic energies in this study. As the silt fraction has a lower standard deviation (SD = 5.81) and correlation coefficient (CV = 0.09) than the clay (SD = 9.14, CV = 0.57) and sand fractions (SD = 11.68, CV = 0.52). We used the latter fractions as well as the MPS as key proxies for AM variation in this study.

Generally, with increases in climate humidity and temperature, enhanced leaching leads to decreased contents of Na_2O and K_2O with little change in Al_2O_3, thus yielding higher CIAm values (Chen et al., 2008; Xiong et al., 2018). However, this inference is subject to several caveats (Shao and Yang, 2012). First, with enhanced physical weathering (i.e., greater soil erosion and sediment yield), the time for chemical weathering can be shortened, thus reducing observed chemical weathering intensity. Second, owing to poor drainage in karst depressions, Na_2O and K_2O in clays washed from the surrounding mountains can build up, leading to lower CIAm values. We infer that the CIAm of the present study units are useful proxies for changes in the AM, with strong AM could correspond to weaker values of CIAm.

Paleoclimate change in Southwest China was dominated by AM-influenced low-latitude hydroclimate variation. The composite cave stalagmite $\delta^{18}O$ record for Southwest China (Fig. 7A; Cheng et al., 2016) can be used as a standard for Asian Monsoon intensity, with lower $\delta^{18}O$ implying higher spatially integrated or summer monsoonal rainfall (Cheng et al., 2016; Yuan et al., 2004). Other proxies such as grain size and elemental concentrations were used to investigate the relationships between these proxies and hydroclimate changes in this study. Good correlations between these proxies and the composite cave $\delta^{18}O$ record (Cheng et al., 2016) suggest that AM precipitation was a crucial modulator of the geochemical and geophysical properties of karst depression deposits. The $\delta^{18}O$ record exhibits a significant positive correlation with the CIAm (Fig. 7B) since the Late Pleistocene, while displaying weaker negative correlation with clay content (Fig. 7C), as well as weaker positive correlations with sand content (Fig. 7D) and mean particle size (MPS; Fig. 7E) of the depression deposits prior to the Holocene, providing compelling evidence for a close causal relationship among these variables.

Secular variation in the CIAm, sand fraction and MPS are in-phase with $\delta^{18}O$, while the clay fraction is anti-phased. This means that higher CIAm, sand fraction and MPS, and lower clay fraction occurred during relatively drier intervals characterized by more positive $\delta^{18}O$, whereas lower CIAm, sand fraction and MPS, and higher clay fraction were associated with wetter periods characterized by more negative $\delta^{18}O$. We infer that, within the study interval, increased values of $\delta^{18}O$ correlate with weakened monsoonal precipitation. In this context, we infer that surface runoff decreased, leading to reduced transport of elements such as K_2O, Na_2O and CaO into depressions with poor drainage capacity, and thus resulting in higher CIAm values. As clay-sized particles are prone to be transported as aggregates (Schieber et al., 2007), decreased surface runoff led to decreased clay content. With a relative decrease in the clay fraction, the sand fraction and MPS would automatically increase, and vice versa.

Secular variation in the paleoenvironmental profiles of the study units can be subdivided into four stages (Fig. 7): Stage I (ca. 34–24 ka), Stage II (24–16 ka), Stage III (16–8 ka), and Stage IV (8 ka-present). Stage I is marked by increases of $\delta^{18}O$, CIAm, sand fraction and MPS. Stage II exhibits relative stability for all proxies. During these stages, precipitation was a dominant control, and vegetation cover (as proxied by $\delta^{13}C_{org}$) and paleotemperature were relatively stable (Fig. 6A), with $\delta^{18}O$ (Fig. 7A) exhibiting a strong correlation to other proxies (Fig. 7B-E). During Stage III, $\delta^{18}O$ began to decrease, reflecting an increase in monsoonal precipitation, which led to lower CIAm, sand fraction, and MPS, as well as an increased clay fraction. During Stage IV, $\delta^{18}O$, CIAm, sand fraction, and MPS increased again, and the clay fraction decreased further. All of these phenomena are in line with the hypothesis proposed above, that weakened monsoonal precipitation in the study area resulted in higher CIAm values, decreased clay content, increased sand content and MPS, and vice versa.

Human-induced vegetation changes and anthropogenic activities may have reduced the influence of hydroclimate on the properties of karst depression deposits during stages III and IV. $\delta^{13}C_{org}$ began to increase around 16.8 ka (Fig. 7F), while the clay and sand fractions, as well as MPS, deviated from the $\delta^{18}O$ trend around 11.7 ka (Cheng et al., 2016). At ca. 4 ka, an abrupt increase in MPS and sand fraction occurred. The increase in $\delta^{13}C$ indicates an expansion of C_4 grassland relative to C_3 woodlands in the study area, which is consistent with the reconstructed vegetation cover from a nearby area in Guangdong Province (Wang et al., 2007). Notably, the turning point of $\delta^{13}C$ at ca. 16.8 ka coincides with the timing of Heinrich Stadial 1 (H1 event) (Stager et al., 2011), while the turning points of particle sizes and fractions at ca. 11.7 ka align with the termination of the Younger Dryas (YD) event (Cheng et al., 2020). Therefore, we suggest that vegetation changes since the Early Holocene and increased anthropogenic activities during the Late Holocene may have reduced the influence of hydroclimate on the properties of the depression deposits in a longer-term pattern.

5.3. *Anthropogenic activities since the Late Holocene*

The “early anthropogenic hypothesis” (EAH) proposes that early agriculturalists transformed planet Earth through land-use changes starting at ca. 5 ka, and through expanded farming activities and livestock tending after ca. 3 ka (Ruddiman, 2003; Ruddiman et al., 2020). Previous work has shown that anthropogenic activities (such as population growth, agricultural expansion, and wars) became sufficiently intense to begin to change land surfaces in China as early as 5–3 ka (Jenny et al., 2019; Zhang et al., 2022). Investigations of early Neolithic to Iron Age archaeological sites have revealed a ramping up of anthropogenic activities in China between ca. 4 and 2.5 ka, with commensurate effects on the regional environment (Hosner et al., 2016). As a consequence of agriculture or deforestation, soil erosional rate under these anthropogenic activities could be several orders of magnitude higher than that under natural conditions (Feng et al., 2016; Renard, 1997; Wischmeier and Smith, 1978; Zhang et al., 2022). Nevertheless, disentangling anthropogenic impacts from other natural impacts during the Holocene is not always straightforward, as early anthropogenic impacts were frequently limited and spatially variable (Cheng et al., 2018; Rothacker et al., 2018).

During the Late Holocene, the influence of enhanced anthropogenic activities on karst sediment properties may have come to predominate over that of paleoclimatic conditions in the study area. In this study, multiproxies of the depression deposits (Figs. 6D, 7C-E, 8A-B) exhibit substantial change during the Late Holocene (ca. 4 ka-present), while less significant fluctuations in earlier time before the Holocene Optimum (Fig. 8A-B). Although there were slight decreases in MPS (Fig. 8A) and

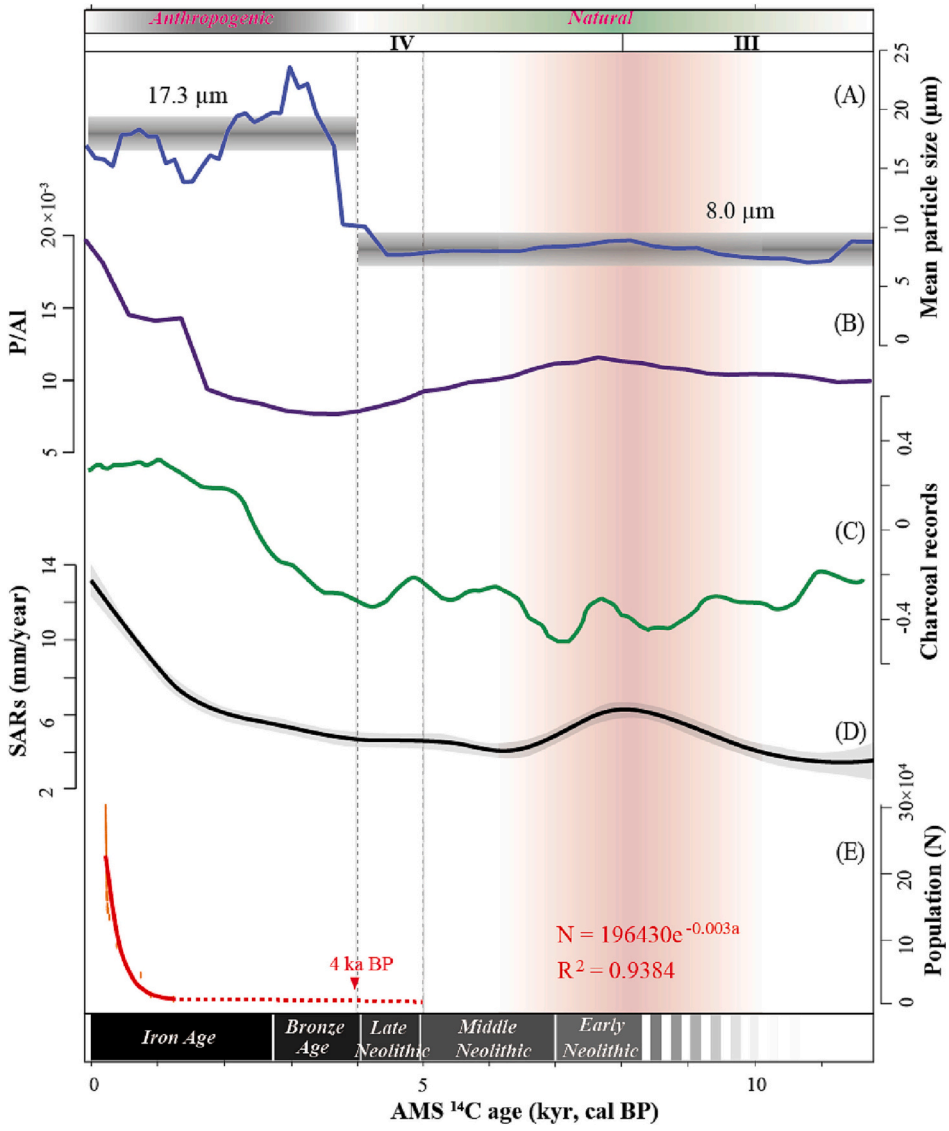

Fig. 8. Anthropogenic factors. (A) and (B) Mean particle size (MPS) and element ratio P/Al (this study); (C) charcoal flux from across China (Xu et al., 2021); (D) sediment accumulation rates (SARs) from lakes and peatlands across China (Zhang et al., 2022); (E) human population of study area extracted from historical records of the Rong'an County (Chen, 1996).

element P (Fig. 8B) after the Holocene Optimum, the MPS after ca. 4 ka was 9.3 μm larger than those influenced by paleoclimate change before this time (Fig. 8A). The abrupt changes of these proxies at ca. 4 ka indicate the impact of anthropogenic activities on environmental conditions increased markedly since the end of the Late Neolithic. Previous studies have concluded that increases in charcoal fluxes (Fig. 8C) across China since ca. 4.5 ka were due to intensified large-scale land clearance and energy harvesting by humans for mining and smelting of copper and iron during the Bronze and Iron Ages (Li et al., 2011; Pei et al., 2020; Xu et al., 2021), and this conclusion is compatible with the findings of the present study. Moreover, the findings of this study are also consistent with the gradual increase in SARs (Fig. 8D) at the Late Neolithic (ca. 4–5 ka) in lakes and peatlands of Southwest China (Zhang et al., 2022).

The geometric (exponential) model of regional population growth also supports increasing influence of anthropogenic activities since the Late Holocene. Based on the history of Rong'an County (Chen, 1996), historical population records extend back to ca. 2.8 ka. By using a geometric (exponential) model of regional population growth, we infer that population numbers were low during the Middle Holocene (Fig. 8E). From the perspective of population size, anthropogenic activities are likely to have overtaken natural factors as the dominant driver of environmental change during the Late Holocene. Our data suggest that 4–5 ka was the key transitional period during which this shift from dominantly natural to dominantly anthropogenic influences occurred.

Overall, the evidences (geophysical, geochemical and biological) in this work supports the EAH hypothesis and the concepts that “the deep roots” of anthropogenic factors have played a significant role in modulating Earth's surface environment (Stephens et al., 2019). Certainly, these results were based on limited records, and more high-resolution multiproxy studies will be needed in the future.

6. Conclusions

This is the one of the first studies to combine radiocarbon dating and multiproxy analysis of karst depression deposits with the goals of investigating the long-term history of paleoclimate change, and of evaluating the timing of anthropogenic activities in modulating Earth's surface environment in a typical karst catchment of Southwest China. This paper suggests that karst depression deposits can serve as suitable

archaeological and paleoclimatic geoarchives, particularly when investigated with multiproxy analyses. Although there are intrinsic defects of dating the karst depression sediment sequences in this study, by using dense AMS ^{14}C dates along multiple depositional sequences and their correlations, well-constrained age-depth models can be developed.

In this research, by comparison of multiproxies from the depression deposits, as well as other high-resolution georecords reported by previous studies, we have shown that paleoclimate change was the main modulator of paleoenvironmental changes and control on vegetation cover during the Early (ca. 12–8 ka) and Middle (ca. 8–4 ka) Holocene. Since the Late Holocene (ca. 5–4 ka), the impacts of anthropogenic activities, especially soil tillage, have overwhelmed natural factors. This work supports the EAH hypothesis and the concepts that anthropogenic factors have played a key role in modulating Earth's surface environment during the Late Holocene.

Author contributions

Jiang, Y.J. designed the research and revised the manuscript. Tian, X. wrote the first version of the manuscript. Luo, S.E. contributed to the particle size and TOC measurements. Long, X.Y., Cao, M., Li, J., Sun, Y. C., Zeng, S.B., Wu, Z., Liu, C., Lei, L.D. and Algeo, T.J. provided technical support in geochemical, geophysical and biological analysis. All authors discussed the results and provided ideas to the manuscript.

Declaration of Competing Interest

The authors declare that they have no known competing financial interests or personal relationships that could have appeared to influence the work reported in this paper.

Data availability

Data will be made available on request.

Acknowledgments

This work was supported by the Chongqing Municipal Science and Technology Commission Fellowship Fund (Grant No. 2022YSZX-JCX0008CSTB) and the National Key Research and Developmental Program of China (2016YFC0502306) granted to Jiang, Y.J.; The National Natural Science Foundation of China (Grant No. 42202108) and the Open Project Program of Chongqing Key Laboratory of Karst Environment (Grant No. Cqk202102) granted to Tian, X.. We express our gratitude to Qiong Xiao, Yongli Guo and Ying Miao from the Institute of Karst Geology, Chinese Academy of Geological Sciences for their valuable support in field sample collection and provision of vehicles and expenses. We also thank Ran Huang and Jinjiang Pan from Southwest University for their assistance with sample collecting and sorting.

Appendix A. Supplementary data

Supplementary data to this article can be found online at https://doi.org/10.1016/j.palaeo.2023.111654.

References

Arnaud, F., Révillon, S., Debret, M., Revel, M., Chapron, E., Jacob, J., Giguet-Covex, C., Poulenard, J., Magny, M., 2012. Lake Bourget regional erosion patterns reconstruction reveals Holocene NW European Alps soil evolution and paleohydrology. Quat. Sci. Rev. 51, 81–92. https://doi.org/10.1016/j.quascirev.2012.07.025.

Bai, X.Y., Zhang, X.B., Chen, H., He, Y.B., 2010. Using Cs-137 fingerprinting technique to estimate sediment deposition and erosion rates from Yongkang depression in the karst region of Southwest China. Land Degrad. Dev. 21, 474–479. https://doi.org/10.1002/ldr.983.

Blaauw, M., 2010. Methods and code for 'classical' age-modelling of radiocarbon sequences. Quat. Geochronol. 5, 512–518. https://doi.org/10.1016/j.quageo.2010.01.002.

Chen, C., 15 co-authors, 2021. Karst hydrological changes during the Late-Holocene in Southwestern China. Quat. Sci. Rev. 258, 106865 https://doi.org/10.1016/j.quascirev.2021.106865.

Chen, J.L., 1996. The annals of Rong'an County, first edition. Guangxi People's Publishing House, Guangxi (in Chinese).

Chen, Y., Li, X., Han, Z., Yang, S., Wang, Y., Yang, D., 2008. Chemical weathering intensity and element migration features of the Xiashu loess profile in Zhenjiang, Jiangsu Province. J. Geogr. Sci. 18, 341–352. https://doi.org/10.1007/s11442-008-0341-9.

Cheng, H., Edwards, R.L., Sinha, A., Spötl, C., Yi, L., Chen, S., Kelly, M., Kathayat, G., Wang, X., Li, X., 2016. The asian monsoon over the past 640,000 years and ice age terminations. Nature 534, 640–646. https://doi.org/10.1038/nature18591.

Cheng, H., 14 co-authors, 2018. Atmospheric C-14/C-12 changes during the last glacial period from Hulu Cave. Science 362, 1293–1297. https://doi.org/10.1126/science.aau0747.

Cheng, H., Zhang, H., Spol, C., Baker, J., Edwards, R.L., 2020. Timing and structure of the Younger Dryas event and its underlying climate dynamics. Proc. Natl. Acad. Sci. USA 117, 23408–23417. https://doi.org/10.1073/pnas.2007869117.

Cheng, Z., Weng, C., Guo, J., Dai, L., Zhou, Z., 2018b. Vegetation responses to late Quaternary climate change in a biodiversity hotspot, the three parallel Rivers region in southwestern China. Palaeogeogr. Palaeoclimatol. Palaeoecol. 491, 10–20. https://doi.org/10.1016/j.palaeo.2017.11.032.

Cheng, Z., Weng, C., Steinke, S., Mohtadi, M., 2018c. Anthropogenic modification of vegetated landscapes in southern China from 6,000 years ago. Nat. Geosci. 11, 939–943. https://doi.org/10.1038/s41561-018-0250-1.

China National Environment Monitoring Centre, 1990. Background Value of Soilelements in China. China Environmental Science Press, Beijing (in Chinese).

Feng, T., Chen, H., Polyakov, V.O., Wang, K., Zhang, X., Zhang, W., 2016. Soil erosion rates in two karst peak-cluster depression basins of Northwest Guangxi, China: Comparison of the RUSLE model with 137Cs measurements. Geomorphology 253, 217–224. https://doi.org/10.1016/j.geomorph.2015.10.013.

Fuller, D.Q., Qin, L., Harvey, E., 2008. Evidence for a late onset of agriculture in the Lower Yangtze region and challenges for an archaeobotany of rice. In: Ross, M. (Ed.), Past Human Migrations in East Asia. Routledge, New York, pp. 72–115.

Ge, J., Deng, C., Wang, Y., Shao, Q., Zhou, X., Xing, S., Pang, H., Jin, C., 2020. Climate-influenced cave deposition and human occupation during the Pleistocene in Zhiren Cave, Southwest China. Quat. Int. 559, 14–23. https://doi.org/10.1016/j.quaint.2020.01.018.

Guedes, J.D.A., Jiang, M., He, K., Wu, X., Jiang, Z., 2013. Site of Baodun yields earliest evidence for the spread of rice and foxtail millet agriculture to south-west China. Antiquity 87, 758–771. https://doi.org/10.1017/S0003598x00049449.

Guo, Z.T., 11 co-authors, 2008. A major reorganization of Asian climate by the early Miocene. Clim. Past 4, 153–174. https://doi.org/10.5194/cp-4-153-2008.

Heaton, T.J., Bard, E., Ramsey, C.B., Butzin, M., Koehler, P., Muscheler, R., Reimer, P.J., Wacker, L., 2021. Radiocarbon: a key tracer for studying Earth's dynamo, climate system, carbon cycle, and Sun. Science 374, eabd7096. https://doi.org/10.1126/science.abd7096.

Hosner, D., Wagner, M., Tarasov, P.E., Chen, X., Leipe, C., 2016. Spatiotemporal distribution patterns of archaeological sites in China during the Neolithic and Bronze Age: an overview. The Holocene 26, 1576–1593. https://doi.org/10.1177/0959683616641743.

Jenny, J.P., Koirala, S., Gregory-Eaves, I., Francus, P., Niemann, C., Ahrens, B., Brovkin, V., Baud, A., Aek, O., Normandeau, A., 2019. Human and climate global-scale imprint on sediment transfer during the Holocene. Proceedings of the National Academy of Sciences (U.S.A.) 116, 22972. https://doi.org/10.1073/pnas.1908179116.

Jiang, Z., Lian, Y., Qin, X., 2014. Rocky desertification in Southwest China: Impacts, causes, and restoration. Earth Sci. Rev. 132, 1–12. https://doi.org/10.1016/j.earscirev.2014.01.005.

Li, J.Y., Li, H.C., Li, T.Y., Mii, H.S., Yu, T.L., Shen, C.C., Xu, X., 2017. High-resolution δ18O and δ13C records of an AMS 14C and 230Th/U dated stalagmite from Xinya Cave in Chongqing: climate and vegetation change during the late Holocene. Quat. Int. 447, 75–88. https://doi.org/10.1016/j.quaint.2017.06.075.

Li, Q., Wu, H., Yu, Y., Sun, A., Luo, Y., 2019. Quantifying regional vegetation changes in China during three contrasting temperature intervals since the last glacial maximum. J. Asian Earth Sci. 174, 23–36. https://doi.org/10.1016/j.jseaes.2018.10.013.

Li, T., Li, H., Xiang, X., Kuo, T.-S., Li, J., Zhou, F., Chen, H., Peng, L., 2012. Transportation characteristics of δ13C in the plants-soil-bedrock-cave system in Chongqing karst area. Sci. China Earth Sci. 55, 685–694. https://doi.org/10.1007/s11430-011-4294-y.

Li, X., Sun, N., Dodson, J., Ji, M., Zhao, K., Zhou, X., 2011. The impact of early smelting on the environment of Huoshiliang in Hexi Corridor, NW China, as recorded by fossil charcoal and chemical elements. Palaeogeogr. Palaeoclimatol. Palaeoecol. 305, 329–336. https://doi.org/10.1016/j.palaeo.2011.03.015.

Liu, J., Algeo, T.J., Yang, H., Pan, J., Tang, C., Huang, J., Xie, S., 2018. Changes in vegetation type on the Chinese Loess Plateau since 75 ka related to East Asian Summer Monsoon variation. Palaeogeogr. Palaeoclimatol. Palaeoecol. 510, 124–139. https://doi.org/10.1016/j.palaeo.2018.02.030.

Lu, H.Y., An, Z.S., 1999. Comparison of grain-size distribution of red clay and loess-paleosol deposits in Chinese Loess Plateau. Acta Sedimentol. Sin. 17 (7) https://doi.org/10.3969/j.issn.1000-0550.1999.02.011 (in Chinese with English abstract).

Lu, H.Y., Guo, Z.T., 2014. Evolution of the monsoon and dry climate in East Asia during late Cenozoic: a review. Sci. China Earth Sci. 57, 70–79. https://doi.org/10.1007/s11430-013-4790-3.
Marwick, B., 2005. Element concentrations and magnetic susceptibility of anthrosols: Indicators of prehistoric human occupation in the inland Pilbara, Western Australia. J. Archaeol. Sci. 32, 1357–1368. https://doi.org/10.1016/j.jas.2005.03.009.
Meyer, L.D., Line, D.E., Harmon, W.C., 1992. Size characteristics of sediment from agricultural soils. J. Soil Water Conserv. 47, 107–111.
Monge, G., Jimenez-Espejo, F.J., Pozo, M., Carretero, M.I., Barroso, C., 2016. A geochemical multi-proxy approach for anthropogenic processes in a Middle-Upper Pleistocene endokarstic deposit. Quat. Int. 407, 140–149. https://doi.org/10.1016/j.quaint.2016.02.004.
Mottl, O., 13 co-authors, 2021. Global acceleration in rates of vegetation change over the past 18,000 years. Science 372, 860–864. https://doi.org/10.1126/science.abg1685.
Nesbitt, H.W., Young, G.M., 1982. Early Proterozoic climates and plate motions inferred from major element chemistry of lutites. Nature 299, 715–717. https://doi.org/10.1038/299715a0.
Ni, J., Yu, G., Harrison, S.P., Prentice, I.C., 2010. Palaeovegetation in China during the late Quaternary: Biome reconstructions based on a global scheme of plant functional types. Palaeogeogr. Palaeoclimatol. Palaeoecol. 289, 44–61. https://doi.org/10.1016/j.palaeo.2010.02.008.
Oonk, S., Slomp, C.P., Huisman, D.J., 2009. Geochemistry as an aid in archaeological prospection and site interpretation: current issues and research directions. Archaeol. Prospect. 16, 35–51. https://doi.org/10.1002/arp.344.
Pei, W., Wan, S., Clift, P.D., Dong, J., Liu, X., Lu, J., Tan, Y., Shi, X., Li, A., 2020. Human impact overwhelms long-term climate control of fire in the Yangtze River Basin since 3.0 ka BP. Quat. Sci. Rev. 230, 106165 https://doi.org/10.1016/j.quascirev.2020.106165.
Peng, Y., Xiao, J., Nakamura, T., Liu, B., Inouchi, Y., 2005. Holocene East asian monsoonal precipitation pattern revealed by grain-size distribution of core sediments of Daihai Lake in Inner Mongolia of north-Central China. Earth Planet. Sci. Lett. 233, 467–479. https://doi.org/10.1016/j.epsl.2005.02.022.
Qu, C.C., Ren, W.Y., Li, X.X., Cai, P., Chen, W.L., Huang, Q.Y., 2022. Revisit soil organic matter. Chin. Sci. Bull. 67, 913–923. https://doi.org/10.1360/TB-2021-0704 (in Chinese with English abstract).
Reimer, P.J., 41 co-authors, 2020. The intcal20 northern hemisphere radiocarbon age calibration curve (0–55 cal BP). Radiocarbon 62, 725–757. https://doi.org/10.1017/rdc.2020.41.
Ren, G., 2007. Changes in forest cover in China during the Holocene. Veg. Hist. Archaeobot. 16, 119–126. https://doi.org/10.1007/s00334-006-0075-5.
Renard, K.G., 1997. Predicting Soil Erosion by Water: A Guide to Conservation Planning with the Revised Universal Soil Loss Equation (RUSLE). United States Government Printing, Washington.
Rienzi, E.A., Fox, J.F., Grove, J.H., Matocha, C.J., 2013. Interrill erosion in soils with different land uses: the kinetic energy wetting effect on temporal particle size distribution. Catena 107, 130–138. https://doi.org/10.1016/j.catena.2013.02.007.
Rothacker, L., Dosseto, A., Francke, A., Chivas, A.R., Vigier, N., Kotarba-Morley, A.M., Menozzi, D., 2018. Impact of climate change and human activity on soil landscapes over the past 12,300 years. Sci. Rep. 8, 247. https://doi.org/10.1038/s41598-017-18603-4.
Ruddiman, W.F., 2003. The anthropogenic greenhouse era began thousands of years ago. Clim. Chang. 61, 261–293. https://doi.org/10.1023/B:CLIM.0000004577.17928.fa.
Ruddiman, W.F., He, F., Vavrus, S.J., Kutzbach, J.E., 2020. The early anthropogenic hypothesis: a review. Quat. Sci. Rev. 240, 106386 https://doi.org/10.1016/j.quascirev.2020.106386.
Schieber, J., Southard, J., Thaisen, K., 2007. Accretion of mudstone beds from migrating floccule ripples. Science 318, 1760–1763. https://doi.org/10.1126/science.1147001.
Schlezinger, D.R., Howes, B.L., 2000. Organic phosphorus and elemental ratios as indicators of prehistoric human occupation. J. Archaeol. Sci. 27, 479–492. https://doi.org/10.1006/jasc.1999.0464.
Shao, J., Yang, S., 2012. Does chemical index of alteration (CIA) reflect silicate weathering and monsoonal climate in the Changjiang River basin? Chin. Sci. Bull. 57, 1178–1187. https://doi.org/10.1007/s11434-011-4954-5.
Siart, C., Hecht, S., Holzhauer, I., Altherr, R., Meyer, H.P., Schukraft, G., Eitel, B., Bubenzer, O., Panagiotopoulos, D., 2010. Karst depressions as geoarchaeological archives: the palaeoenvironmental reconstruction of Zominthos (Central Crete), based on geophysical prospection, sedimentological investigations and GIS. Quat. Int. 216, 75–92. https://doi.org/10.1016/j.quaint.2009.06.020.
Stager, J.C., Ryves, D.B., Chase, B.M., Pausata, F.S.R., 2011. Catastrophic Drought in the Afro-Asian Monsoon Region during Heinrich Event 1. Science 331, 1299–1302. https://doi.org/10.1126/science.1198322.
Stephens, L., 120 co-authors, 2019. Archaeological assessment reveals Earth's early transformation through land use. Science 365, 897–902. https://doi.org/10.1126/science.aax1192.
Sun, W., Song, J., Yang, W., Zheng, Y., Li, C., Kuang, D., 2020. Distribution of carbonate rocks and variation analysis of karst water resources in China. Carbon. Evap. 35, 121. https://doi.org/10.1007/s13146-020-00657-7.
Sun, X., Wu, Y., Qiao, Y., Walker, D., 1986. Late Pleistocene and Holocene vegetation history at Kunming, Yunnan province, Southwest China. J. Biogeogr. 13, 441–476. https://doi.org/10.2307/2844967.
Sun, Y., An, Z., Clemens, S.C., Bloemendal, J., Vandenberghe, J., 2010. Seven million years of wind and precipitation variability on the Chinese Loess Plateau. Earth Planet. Sci. Lett. 297, 525–535. https://doi.org/10.1016/j.epsl.2010.07.004.
Syvitski, J., 17 co-authors, 2020. Extraordinary human energy consumption and resultant geological impacts beginning around 1950 CE initiated the proposed Anthropocene Epoch. Commun. Earth Environ. 1, 1–13. https://doi.org/10.1038/s43247-020-00029-y.
Tiessen, H., 1996. Phosphorous in the global environment: transfers, cycles and management. Oceanogr. Lit. Rev. 7, 742. https://doi.org/10.1016/0016-7061(96)00046-8.
Wan, S., 11 co-authors, 2015. Human impact overwhelms long-term climate control of weathering and erosion in Southwest China. Geology 43, 439–442. https://doi.org/10.1130/g36570.1.
Wang, L., Shi, Z.H., 2015. Size selectivity of eroded sediment associated with soil texture on steep slopes. Soil Sci. Soc. Am. J. 79, 917–929. https://doi.org/10.2136/sssaj2014.10.0415.
Wang, L., Shi, Z.H., Wang, J., Fang, N.F., Wu, G.L., Zhang, H.Y., 2014. Rainfall kinetic energy controlling erosion processes and sediment sorting on steep hillslopes: a case study of clay loam soil from the Loess Plateau, China. J. Hydrol. 512, 168–176. https://doi.org/10.1016/j.jhydrol.2014.02.066.
Wang, S., Lu, H., Liu, J., Negendank, J., 2007. Early Holocene climate optimum revealed by high-resolution pollen record from Huguangyan Maar Lake. Chin. Sci. Bull. 52, 1285–1291. https://doi.org/10.1007/s11434-007-0419-2.
Waters, C.N., Turner, S.D., 2022. Defining the onset of the Anthropocene. Science 378, 706–708. https://doi.org/10.1126/science.ade2310.
Wei, G., Li, X.H., Liu, Y., Shao, L., Liang, X., 2006. Geochemical record of chemical weathering and monsoon climate change since the early Miocene in the South China Sea. Paleoceanography 21, PA4214. https://doi.org/10.1029/2006PA001300.
Wischmeier, W.H., Smith, D.D., 1978. Predicting Rainfall Erosion Losses: A Guide to Conservation Planning. USDA Agriculture Handbook, Washington, D.C.
Wu, S., 2021. tudy on Soil and Water Process in Different Governance Modes of Typical Karst Peak-Cluster Depression in Guangxi. Guilin University of Technology, Guangxi (in Chinese with English abstract).
Wu, Y., Li, T.Y., Yu, T.L., Shen, C.C., Chen, C.J., Zhang, J., Li, J.Y., Wang, T., Huang, R., Xiao, S.Y., 2020. Variation of the asian summer monsoon since the last glacial-interglacial recorded in a stalagmite from Southwest China. Quat. Sci. Rev. 234, 106261 https://doi.org/10.1016/j.quascirev.2020.106261.
Xiong, K., Yin, C., Ji, H., 2018. Soil erosion and chemical weathering in a region with typical karst topography. Environ. Earth Sci. 77, 1–14. https://doi.org/10.1007/s12665-018-7675-0.
Xu, X., Li, F., Lin, Z., Song, X., 2021. Holocene fire history in China: responses to climate change and human activities. Sci. Total Environ. 753, 142019 https://doi.org/10.1016/j.scitotenv.2020.142019.
Yuan, D., Cheng, H., Edwards, R.L., Dykoski, C.A., Kelly, M.J., Zhang, M., Qing, J., Lin, Y., Wang, Y., Wu, J., 2004. Timing, duration, and transitions of the last interglacial asian monsoon. Science 304, 575–578. https://doi.org/10.1126/science.1091220.
Zhang, F., Li, S., Sun, C., Li, W., Zhao, X., Chen, Z., Nie, T., Chen, Y., Li, X., 2022. Human Impacts Overwhelmed Hydroclimate Control of Soil erosion in China 5,000 years Ago. Geophys. Res. Lett. 49, e2021GL096983 https://doi.org/10.1029/2021GL096983.
Zhang, Y., Long, Y., Zhang, X., Pei, Z., Lu, X., Wu, Z., Xu, M., Yang, H., Cheng, P., 2020. Using depression deposits to reconstruct human impact on sediment yields from a small karst catchment over the past 600 years. Geoderma 363, 114168. https://doi.org/10.1016/j.geoderma.2019.114168.
Zhao, C., 18 co-authors, 2021. Possible obliquity-forced warmth in southern Asia during the last glacial stage. Sci. Bull. 66, 1136–1145. https://doi.org/10.1016/j.scib.2020.11.016.
Zhao, Y., Yu, Z., Chen, F., Zhang, J., Yang, B., 2009. Vegetation response to Holocene climate change in monsoon-influenced region of China. Earth Sci. Rev. 97, 242–256. https://doi.org/10.1016/j.earscirev.2009.10.007.
Zhao, Z., 2010. New data and new issues for the study of origin of rice agriculture in China. Archaeol. Anthropol. Sci. 2, 99–105. https://doi.org/10.1007/s12520-010-0028-x.
Zhou, W., Chui, Y., Yang, L., Cheng, P., Chen, N., Ming, G., Hu, Y., Li, W., Lu, X., 2022. 14C geochronology and radiocarbon reservoir effect of reviewed lakes study in China. Radiocarbon 64, 833–844. https://doi.org/10.1017/RDC.2021.92.
Zhou, Y., Zhang, W., Cheng, X., Harris, W., Schaeffer, S.M., Xu, X., Zhao, B., 2019. Factors affecting C-13 enrichment of vegetation and soil in temperate grasslands in Inner Mongolia, China. J. Soils Sediments 19, 2190–2199. https://doi.org/10.1007/s11368-019-02248-z.